Fatigue & Fracture of Engineering Materials & Structures 1998; **21**: 885–901

A MODIFIED STRIP-YIELD MODEL FOR PREDICTION OF PLASTICITY-INDUCED CLOSURE IN SURFACE FLAWS

S. R. DANIEWICZ

Mississippi State University, Department of Mechanical Engineering, P. O. Drawer ME, Mississippi State, MS 39762-5925, USA

Received in final form March 1998

Abstract—A slice synthesis methodology is developed and used to construct a modified strip-yield model for the semielliptical surface flaw, enabling prediction of plasticity-induced closure along the crack front and subsequent fatigue crack growth. A mathematical description of the model is presented. Slice synthesis methodologies have previously been limited to stress intensity factor and elastic crack displacement computation. Predictions of flaw shape evolution under cyclic loading are compared with experimental data for aluminium alloy specimens under uniform constant amplitude loading with $R = 0.1$, 0.3 and 0.6. Model predictions are shown to correlate well with experimental data. An empirical correlation of relative crack opening stress with applied R ratio from the literature is shown to underestimate the level of closure at the deepest point of penetration when compared with the model predictions.

Keywords—Fatigue; Crack propagation; Surface cracks; Stress analysis; Crack closure.

NOMENCLATURE

a = crack depth
c = half-surface crack length
E = modulus of elasticity
K = stress intensity factor
$m(x, \mathrm{a})$ = weight function
N = number of cycles
$P(x, y)$ = shear traction
R = stress ratio
S_{max} = maximum applied stress
S_o = crack opening stress
S_y = yield strength
S_u = ultimate tensile strength
t = specimen thickness
U = closure parameter
w = crack surface displacement
W = specimen width
α = constraint factor
β_R = relative closure parameter
ΔK, ΔK_{eff} = stress and effective stress intensity factor range
Φ = complete elliptical integral of the second kind
ν = Poisson's ratio
ρ = plastic zone size
σ_0 = flow stress

INTRODUCTION

The part-through semielliptical surface flaw is commonly encountered in engineering practice. Models enabling the accurate prediction of the growth of this type of flaw under cyclic loading represent an essential element in any damage-tolerant design methodology. In metallic materials, a growing surface flaw will remain closed or partially closed along the crack front for a portion of the applied cyclic load as a consequence of plastically deformed material left in the wake of the

growing crack. Proper characterization of this plasticity-induced crack closure is needed when predicting flaw shape development and growth [1–7].

Surface flaws exhibit a level of closure which varies along the crack front. Both the extent and variation of this closure have not been well characterized. First discussed by Elber [8,9], plasticity-induced fatigue crack closure has attracted the interest of many researchers. Due to the complex nature of the surface flaw, the majority of this research activity has focused on through crack geometries, e.g. the compact tension specimen and the centre-cracked panel. The amount of crack closure information available for surface flaws is relatively small in comparison to that for through cracks.

Modelling the plasticity-induced closure generated by the semi-elliptical surface flaw may be performed using three-dimensional non-linear finite element analysis [10]. However, from an engineering perspective, this type of an approach is impractical. Predominantly developed by Newman [11], modified strip-yield models have found wide application for prediction of crack closure and subsequent fatigue crack growth in planar geometries with through cracks. This is evidenced by the large number of strip-yield modelling efforts reported in the literature [11–23]. While approximate in nature, these type of models exhibit high computational efficiency when compared to more rigorous finite element analyses.

This paper discusses the development and application of a modified strip-yield model for surface flaws under constant amplitude loading. An elastic–perfectly plastic half-space contains a semi-elliptical surface flaw, as shown in Fig. 1. The flaw is assumed to be small, such that the only free

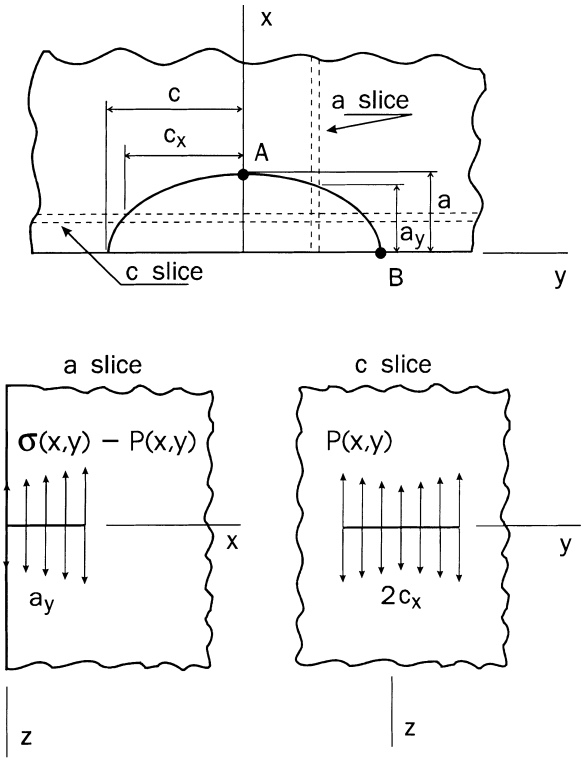

Fig. 1. Slice synthesis model.

surface considered is that at $x = 0$. The flaw is opened with an arbitrary symmetrical applied stress σ_{zz} (x, y).

In the model development process, a slice synthesis methodology [24], previously limited to stress intensity factor and elastic crack surface displacement computation, was extended to allow consideration of localized plastic deformation along the crack front. Using coupled modified strip-yield model analyses, concurrent crack closure assessments for the surface flaw at both points A and B (Fig. 1) were performed. To date, strip-yield modelling of surface flaws has been limited to the prediction of limit loads and plastic zone size [25].

MODIFIED STRIP-YIELD MODEL

Using weight function-based formulations, Wang and Blom [20], and Daniewicz *et al.* [19,21] have generalized the Newman [11] modified strip-yield model to allow treatment of arbitrary planar geometries with through cracks. Such generalizations require a large number of numerical integrations for each increment of crack growth, and computational efficiency may be increased through use of a Gauss–Chebyshev quadrature [26]. A modified strip-yield model utilizing weight functions for planar geometry description forms the basis for development of a model which allows consideration of the surface flaw.

Assuming the surface flaw maintains a semi-elliptical shape while under cyclic loading, a two-parameter description of the surface flaw may be adopted. Attention may then be restricted to crack growth at points A and B (Fig. 1). Using a weight function-based slice synthesis methodology presented by Zhao *et al.* [24], through crack weight functions for two-dimensional bodies may be used to approximate surface flaw stress intensity factors, plastic zone sizes and crack surface displacements. This information permitted the prediction of crack opening behaviour using the algorithm presented by Newman [11]. The slice synthesis methodology was first introduced by Fujimoto [27], and Saff and Sanger [28] for stress intensity factor computation. More recently, it has been used to compute surface crack and corner crack stress intensity factors and crack opening displacements [29,30].

As illustrated in Fig. 1, the behaviour of the surface flaw is synthesized using two groups of through crack slices. The surface flaw is characterized using a crack depth a and length $2c$. The slices situated parallel with the x-axis are denoted as primary slices or a slices, while those aligned parallel with the y-axis are termed spring slices or c slices. Each primary slice constitutes an edge-cracked strip and is assumed to be in a plane stress condition. The slice exhibits a modulus of elasticity E and a flow stress σ_0. The slice has a crack length a_y, as defined by the elliptical shape and given as

$$a_y = a\sqrt{1 - (y/c)^2} \tag{1}$$

Surface flaw stress intensity factors and crack surface displacements may be estimated accurately using these two-dimensional slices if an unknown shear traction $\sigma_{yz} = P(x, y)$ acting between adjacent primary slices is introduced. The material surrounding each primary slice on either side acts to restrain crack surface displacement, and thus this traction acts in a direction opposite to that of the applied stress $\sigma(x, y) = \sigma_{zz}(x, y)$. Consequently, the applied stress on any given primary slice is $\sigma(x, y) - P(x, y)$, as shown in Fig. 1. The stress intensity factor K_a and elastic crack surface displacement $w_a(x, y)$ for an arbitrarily located primary slice resulting from the applied stress

$\sigma(x, y)$ are given by

$$K_a = \int_0^{a_y} [\sigma(\xi, y) - P(\xi, y)] m_a(\xi, a_y)\, d\xi \tag{2}$$

$$w_a(x, y) = \frac{1}{E} \int_x^{a_y} \int_0^{\alpha} [\sigma(\xi, y) - P(\xi, y)] m_a(\xi, \alpha) m_a(x, \alpha)\, d\xi\, d\alpha \tag{3}$$

where the primary slice weight function for an edge crack of length a_y is denoted as $m_a(\xi, a_y)$. The specific weight function used is given in the Appendix. The slice synthesis must be calibrated if it is to function properly. Through a calibration process using an exact solution for an embedded semi-elliptical flaw under uniform tension, it may be shown [24,27] that Eq. (2) will yield an accurate estimate of the surface flaw stress intensity factor at point A if $y = 0$ and a plane strain scaling factor $1/(1 - \nu^2)$ is introduced, where ν represents Poisson's ratio

$$K_A = \frac{1}{1 - \nu^2} \int_0^a [\sigma(\xi, 0) - P(\xi, 0)] m_a(\xi, a)\, d\xi \tag{4}$$

The required mechanical coupling between adjacent primary slices is made possible through the introduction of an additional series of slices denoted as spring slices or c slices. These slices enable the computation of the unknown shear traction through enforcement of compatibility with $w_a = w_c$, where w_c is the spring slice displacement. As shown in Fig. 1, each spring slice constitutes a centre-cracked panel and is assumed to be under a plane stress condition. These slices are parallel to the free surface and exhibit a modulus of elasticity E_S and a flow stress σ_{0S}. Each of the slices has a crack length $2c_x$ with c_x defined from the elliptical shape and given by

$$c_x = c\sqrt{1 - (x/a)^2} \tag{5}$$

Both E_S and σ_{0S} are fictitious quantities defining the level of mechanical coupling between adjacent primary slices. Using the previously discussed calibration process it may be demonstrated [24,27,28] that

$$\frac{E_S}{E} = \left(\frac{\Phi}{1 - \nu^2} - 1 \right) \frac{c}{a} \tag{6}$$

In this expression, Φ represents a complete elliptic integral of the second kind with, for $a/c \leqslant 1$

$$\Phi = \int_0^{\pi/2} [(a/c)^2 \sin^2 \phi + \cos^2 \phi)^{1/2}\, d\phi \tag{7}$$

The determination of the spring slice flow stress σ_{0S} will be considered following an elastic analysis of the spring slice. The spring slice stress intensity factor K_c and elastic crack surface displacement $w_c(x, y)$ resulting from the applied stress $\sigma(x, y)$ are given by

$$K_c = \int_0^{c_x} P(x, \eta) m_c(\eta, c_x)\, d\eta \tag{8}$$

$$w_c(x, y) = \frac{1}{E_S} \int_y^{c_x} \int_0^{\gamma} P(x, \psi) m_c(\psi, \gamma) m_c(y, \gamma)\, d\psi\, d\gamma \tag{9}$$

where the spring slice weight function for a centre-crack with length $2c_x$ under symmetrical loading with $P(x, y) = P(x, -y)$ is denoted as $m_c(\eta, c_x)$. This symmetrical shear traction implies

$\sigma(x, y) = \sigma(x, -y)$. The specific weight function used is given in the Appendix. From the previously mentioned calibration process, it may also be shown that Eq. (8) will yield an accurate estimate of the surface flaw stress intensity factor at point B if $x = 0$ and it is scaled by a factor E/E_S such that

$$K_B = \frac{E}{E_S} \int_0^c P(0, \eta) m_c(\eta, c)\, d\eta \tag{10}$$

Next, consider localized plastic deformation along the crack front, as illustrated in Fig. 2. Using a strip-yield modelling approach, the surface flaw and subsequent plastic zone are treated as an effective crack in an elastic body. The effective surface flaw is characterized using a crack depth a, crack length $2c$, and plastic zones ρ_A and ρ_B. The effective and actual surface flaws are concentric semi-ellipses. As suggested by Dugdale [31], the extent of the plastic zone may be determined if the material flow stress is assumed to act as a compressive cohesive stress applied within the plastic zone. At the effective crack front, the stress is assumed finite with the net stress intensity factor equal to zero. The slice plastic zone sizes $\rho_a = \rho_y$ and $\rho_b = \rho_x$ for slices passing through points A and B may be found using the following relationships which enforce a zero net stress intensity factor at A and B, respectively,

$$\frac{1}{1-\nu^2} \int_0^{a+\rho_a} [\sigma(\xi, 0) - P(\xi, 0)] m_a(\xi, a + \rho_a)\, d\xi - \int_a^{a+\rho_a} \alpha_A \sigma_0 m_a(\xi, a + \rho_a)\, d\xi = 0 \tag{11}$$

$$\int_0^{c+\rho_b} P(0, \eta) m_c(\eta, c + \rho_b)\, d\eta - \int_c^{c+\rho_b} \alpha_B \sigma_{0S} m_c(\eta, c + \rho_b)\, d\eta = 0 \tag{12}$$

A calibration process analogous to that discussed for the elastic crack analysis is necessary to correlate the slice plastic zones ρ_a and ρ_b with the surface crack plastic zone sizes ρ_A and ρ_B, as well as to define the spring slice flow stress σ_{0S}.

When using modified strip-yield models, it is commonly assumed that the cohesive stress within the plastic zone is a constant. In Eqs (11) and (12), α_A and α_B are constraint factors which describe the average stress to flow stress ratio in the plastic zone at points A and B, respectively. In Eq. (11), note that plane strain conditions are enforced by proper selection of the factor α_A, and consequently the plane strain factor $1/(1-\nu^2)$ has not been applied to the second integral representing the stress intensity factor associated with the plastic zone loading. In addition, also note from the first integral that the shear traction has been applied along the entire effective crack length including the plastic zone. Consequently, it is unnecessary to apply the shear traction again within the second integral.

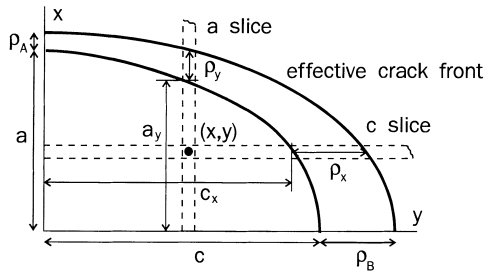

Fig. 2. Crack front localized plastic deformation.

Just as the elastic properties of the spring slice were defined using a calibration process, the flow properties must be defined as well when constructing a strip-yield model for the surface crack. As shown in the Appendix, through a calibration process using an exact strip-yield model solution for an embedded circular flaw under uniform tension, we may write

$$\frac{\sigma_{0S}}{\sigma_0} = \frac{E_S}{E} = \left(\frac{\Phi}{1-\nu^2} - 1\right)\frac{c}{a} \tag{13}$$

In addition, this calibration yields the following correlations between slice plastic zone sizes ρ_a and ρ_b, and surface crack plastic zone sizes ρ_A and ρ_B

$$\frac{\rho_A}{a} = \frac{1}{\dfrac{1}{\ln(1+\rho_a/a)} - 1} \tag{14}$$

$$\frac{\rho_B}{c} = \frac{1}{\dfrac{1}{\ln(1+\rho_b/c)} - 1} \tag{15}$$

Under conditions of small-scale yielding, Eqs (14) and (15) yield $\rho_A = \rho_a$ and $\rho_B = \rho_b$. Equations (11) and (12) constitute a system of non-linear equations for the two unknowns ρ_A and ρ_B. This system was solved iteratively. Note that the shear traction $P(x, y)$ is needed both in the plastic zone as well as throughout the crack, and is thus a function of ρ_A and ρ_B.

Under small-scale yielding conditions, plastic zone sizes computed using Eqs (11)–(15) have been found to coincide with the well-known Dugdale solution $\rho_A = (\pi/8)(K_A/\alpha_A\sigma_0)^2$ and $\rho_B = (\pi/8)(K_B/\alpha_B\sigma_0)^2$. For larger levels of applied load, plastic zone size computations from Ayres [32] were used to further validate the strip-yield model.

Ayres modelled a uniformly loaded surface crack in an elastic–perfectly plastic alloy steel plate with thickness t and a flow stress $\sigma_0 = 1380$ MPa using a finite difference procedure. The aspect ratio a/c and the normalized crack depth a/t were both equal to 0.50. Under a uniform applied stress $S = 0.522\ \sigma_0$, Ayres computed plastic zone sizes in the plane of the crack given by $\rho_A/a \approx 0.080$ and $\rho_B/c \approx 0.040$. These values were reproduced using the strip-yield model with constraint factors $\alpha_A = 1.70$ and $\alpha_B = 1.40$. While constraint factors of 3.0 and 1.0 for plane strain and plane stress, respectively, are typical under small-scale yielding conditions, these constraint factors were considered/realistic given the relatively large magnitude of the applied stress.

Having determined the plastic zone sizes, the crack surface displacements at a point of interest (x, y) resulting from both the applied stress and the plastic zone loading may be derived as demonstrated in the Appendix. These displacements may be written as

$$\begin{aligned} w_a(x, y) = \frac{1}{E}\int_x^{a_y}\left\{\int_0^{\alpha}[\sigma(\xi, y) - P(\xi, y)]m_a(\xi, \alpha)\,d\xi\right\}m_a(x, \alpha)\,d\alpha \\ + \frac{1}{E}\int_{a_y}^{a_y+\rho_y}\left\{\int_0^{\alpha}[\sigma(\xi, y) - P(\xi, y)]m_a(\xi, \alpha)\,d\xi\right. \\ \left. - \int_{a_y}^{\alpha}\alpha_a\sigma_0 m_a(\xi, \alpha)\,d\xi\right\}m_a(x, \alpha)\,d\alpha \end{aligned} \tag{16}$$

$$w_c(x, y) = \frac{1}{E_S}\int_y^{c_x}\left\{\int_0^{\gamma} P(x, \psi)m_c(\psi, \gamma)\,d\psi\right\} m_c(y, \gamma)\,d\gamma + \frac{1}{E_S}\int_{c_x}^{c_x+\rho_x}\left\{\int_0^{\gamma} P(x, \psi)m_c(\psi, \gamma)\,d\psi - \int_{c_x}^{\gamma}\alpha_c\sigma_{0S}m_c(\psi, \gamma)\,d\psi\right\} m_c(y, \gamma)\,d\gamma \quad (17)$$

where α_a and α_c are constraint factors for arbitrarily located primary and spring slices. When these slices are situated such that they pass through points A and B, $\alpha_a = \alpha_A$ and $\alpha_c = \alpha_B$. To ensure compatibility, the displacement from each slice must be equal, with $w_a = w_c$. This condition is used to determine the shear traction, as shown in the Appendix. Following calibration, these slice displacements equal the surface flaw displacement. Also, from Fig. 2

$$\rho_x = (c + \rho_b)\sqrt{1 - x^2/(a + \rho_a)^2} - c\sqrt{1 - x^2/a^2}$$
$$\rho_y = (a + \rho_a)\sqrt{1 - y^2/(c + \rho_b)^2} - a\sqrt{1 - y^2/c^2} \quad (18)$$

Using prescribed constraint factors for points A and B, the constraint factors for an arbitrary location along the crack front are assumed to be given by the following linear relationship

$$\alpha(\varphi) = \frac{\alpha_A - \alpha_B}{\pi/2}\varphi + \alpha_B \quad (19)$$

where two ϕ angles are defined in Fig. 3, with $\cos\phi_x = c_x/c$ and $\sin\phi_y = a_y/a$. Note that for points (x, y) not on the crack perimeter, a unique ϕ_y and ϕ_x are required for the primary and spring slice, respectively, with $\alpha_a = \alpha(\phi_y)$ and $\alpha_c = \alpha(\phi_x)$. For points on the perimeter, $\phi_y = \phi_x$. The linear constraint distribution (in terms of ϕ) along the crack front was assumed solely for simplicity, and no numerical or experimental information exists to support this assumption. The linear distribution may over-represent the plane stress contribution associated with the free surface at point B. Although currently unknown, a more rigorous distribution may involve a crack front dominated by plane strain conditions, with the exception of a small region near point B where the constraint decreases rapidly to a plane stress level. Elastic–plastic finite element analysis represents one potential means of characterizing the distribution of constraint along the crack front. This distribution will also be a function of applied load.

Next, consider the computation of the unknown shear traction $P(x, y)$. For equilibrium, at arbitrary points (x, y) along the crack surface where the primary and spring slices intersect, the

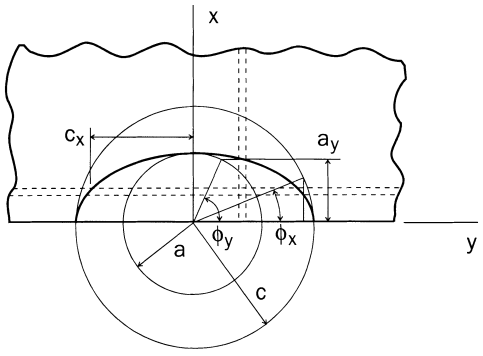

Fig. 3. Crack front angular positions.

total applied stress must be $\sigma(x, y)$. Equilibrium then dictates that each spring slice be subject to an applied stress $P(x, y)$, as shown in Fig. 1. With the primary and spring slices assumed to exhibit a flow stress σ_0 and σ_{0S}, respectively, points of interest (x, y) must be confined within the actual crack boundary (no points in the plastic zone) to avoid a net cohesive stress $-(\sigma_0 + \sigma_{0S})$. In addition, compatibility dictates that the displacement from each slice must be equal, with $w_a = w_c$. As shown in the Appendix, if $P(x, y)$ is assumed to be a linear combination of prescribed basis functions $p_i(x, y)$, compatibility enables the computation of 14 coefficients, λ_i, such that the shear traction is defined as follows [24]

$$P(x, y) = \sum_{i=1}^{14} \lambda_i p_i(x, y) \tag{20}$$

In expanded form this expression may be written as

$$\begin{aligned} P(x, y) = {} & \lambda_1 + \lambda_2(y/c)^{1/3} + \lambda_3(x/a)^{1/3} + \lambda_4(xy/ac)^{1/3} + \lambda_5(y/c) \\ & + \lambda_6(x/a) + \lambda_7(xy/ac) + \lambda_8(y/c)^2 + \lambda_9(x/a)^2 + \lambda_{10}(xy/ac)^2 \\ & + \lambda_{11}(y/c)^3 + \lambda_{12}(x/a)^3 + \lambda_{13}(y/c)^4 + \lambda_{14}(x/a)^4 \end{aligned} \tag{21}$$

The model described thus far may be characterized as a strip-yield model for monotonic loading. With this model, both the extent of the regions exhibiting plastic deformation along the crack front as well as the subsequent crack surface displacements may be determined. For analysis of plasticity-induced crack closure, cyclic loading must be considered, and monotonic strip-yield models must be modified to leave plastically deformed material along the crack surfaces as the crack advances [11]. Using a weight function-based formulation, Daniewicz *et al.* [21] have generalized the Newman modified strip-yield model to allow treatment of arbitrary through crack geometries. With the surface flaw now described in terms of two through cracks through application of the slice synthesis methodology, a surface flaw-modified strip-yield model was constructed using two coupled through crack modified strip-yield analyses. For more detailed discussions concerning modified strip-yield models, see Refs [11,20,21].

Fatigue crack growth rates at points A and B, as shown in Fig. 1, were assumed to be characterized in terms of effective stress intensity factor ranges $(\Delta K_{\text{eff}})_A$ and $(\Delta K_{\text{eff}})_B$

$$\frac{da}{dN} = C_A(\Delta K_{\text{eff}})_A^{n_A} \qquad \frac{dc}{dN} = C_B(\Delta K_{\text{eff}})_B^{n_B} \tag{22}$$

where an effective stress intensity factor range is defined using the maximum applied stress $S_{\max}$ and the computed crack opening stress S_0

$$\Delta K_{\text{eff}} = K(S_{\max}) - K(S_0) \tag{23}$$

Equation (22) may be combined to yield

$$dc = \frac{C_B}{C_A} \frac{(\Delta K_{\text{eff}})_B^{n_B}}{(\Delta K_{\text{eff}})_A^{n_A}} da \tag{24}$$

All required stress intensity factor computations were made using Eqs (4) and (10). Use of these equations resulted in values that were within 2% of those documented by Newman and Raju [33].

Modified strip-yield models were created for a primary slice passing through point A and a spring slice passing through point B. These two models were coupled and utilized concurrently. Figure 2 illustrates a primary and spring slice pair. Note that while numerous pairs were utilized for computation of the shear traction $P(x, y)$, as discussed in the Appendix, only a single primary

and spring slice were used for crack opening stress prediction. From an initial assumed flaw size a_i and c_i, the crack opening stress at point A was first predicted using an assumed increment of crack extension da with d$a = 0.04\rho_A$. The crack opening stress at point B was next computed using an assumed crack growth increment dc. Using Eq. (24), the resulting crack opening stresses were then used to compute a crack growth increment dc. If the computed dc differed from the assumed value, the computed value was used to determine a new crack opening stress at B with this process repeated until convergence was obtained. This procedure was repeated for each crack growth increment da until the prescribed final crack depth a was attained. Use of this methodology enabled the computation of opening stresses for points A and B as a function of current flaw size, as well as a prediction of aspect ratio (a/c) evolution under the prescribed cyclic loading.

MODEL APPLICATION: RESULTS AND DISCUSSION

Crack opening stress predictions for a semicircular crack were compared with predictions from an earlier finite element analysis [10]. Chermahini *et al.* [10] computed crack opening stresses for a surface cracked elastic–perfectly plastic aluminium alloy plate with thickness $t = 25.4$ mm and flow stress $\sigma_0 = 345$ MPa. The plate was loaded under a uniform tension with $S_{max}/\sigma_0 = 0.40$ and $R = 0.1$. The initial surface flaw was semicircular with an aspect ratio of unity and $a = 10.2$ mm. The flaw was assumed to growth such that this aspect ratio was maintained. Four constant amplitude load cycles were modelled in the finite element analysis, with each cycle resulting in a crack growth increment of one element size (0.08 mm). Following application of the four load cycles, crack opening stresses S_0 at A and B were computed with $(S_0)_A/S_{max} \approx 0.134$ and $(S_0)_B/S_{max} \approx 0.200$.

Crack opening stresses from the finite element analysis were compared with predictions from the modified strip-yield model. To enable this comparison, the crack was assumed to maintain a semicircular shape during growth to a depth $a = 10.52$ mm. This required modifying the strip-yield model to enforce da = dc and eliminating the use of Eq. (24). Constraint factors were varied from 1.0 to 3.0 with $\alpha_A \geqslant \alpha_B$. These analyses indicated that the crack opening stress $(S_0)_A$ was a function of α_A alone and independent of α_B with $(S_0)_A = f(\alpha_A)$. Similarly, for the free surface $(S_0)_B = g(\alpha_B)$. In addition, it was observed that the functions f and g were nearly identical, as shown in Fig. 4. Regardless of the constraint factor chosen, predicted opening stress values were larger than the values reported by Chermahini *et al.* [10]. Thus, a poor correlation was observed between the strip-yield model results and those from the finite element analysis. The finite element model-normalized crack opening stress values were significantly lower in magnitude than any predicted by the strip-yield model. In comparison to through crack opening stress values, the finite element model predictions also appear to be small in magnitude. The small opening stresses predicted by the finite element model may be a result of an insufficient degree of mesh refinement such that the crack growth increment (element size) constituted too large a fraction of the plastic zone size under the maximum load. This potential limitation of the finite element model was acknowledged by Chermahini *et al.* [10], who suggested that results from their analyses will show general trends only.

Growth of a semielliptical surface flaw under a constant amplitude uniform stress was next predicted and compared with experimental data [2,3]. Jolles and Tortoriello presented the aspect ratio (a/c) as a function of normalized crack depth (a/t) for a 2024-T351 aluminium alloy plate with thickness $t = 25.4$ mm and width $W = 25.4$ mm (Fig. 5). This plate was loaded under uniform tension with various R ratios and a maximum applied stress $S_{max} = 124$ MPa. Using compact tension specimens, a fatigue crack growth rate exponent $n_A = n_B = n = 3.76$ [Eq. (22)] was found. A typical yield and ultimate strength $S_y = 345$ MPa and $S_u = 482$ MPa were used to compute a

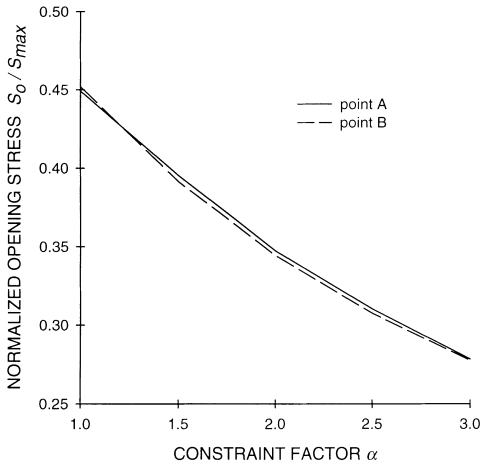

Fig. 4. Effect of constraint on crack opening predictions for a fixed aspect ratio $a/c = 1.0$.

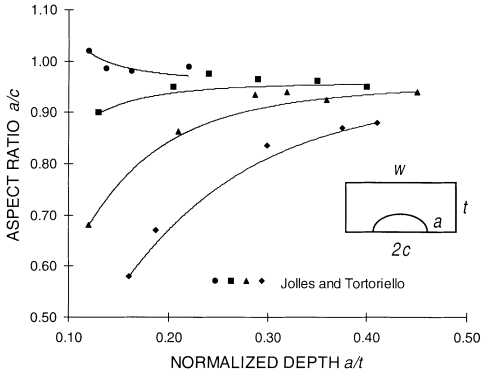

Fig. 5. Predicted and measured aspect ratio evolution, $R = 0.1$.

flow stress σ_0, assumed to be the average of these quantities such that $\sigma_0 = 413$ MPa and $S_{max}/\sigma_0 = 0.30$. From a crack growth perspective, the material was assumed isotropic and the fatigue crack growth rate coefficients C_A and C_B were assumed equal.

Treating the constraint factors α_A and α_B as fitting parameters, the modified strip-yield model was first calibrated using the experimental data with $R = 0.1$. Results from four fatigue tests were used, each exhibiting a different initial aspect ratio and crack depth. Constraint factors $\alpha_A = 3.00$ and $\alpha_B = 2.50$ were found to produce reasonable correlations with the four experiments, as shown in Fig. 5. The constraint factors used will also determine the extent of the crack front plastic zone, as seen from Eqs (11) and (12). For a surface flaw with $a/t = 0.13$, $a/c = 0.90$ and $S_{max}/\sigma_0 = 0.30$, the plastic zone sizes predicted were $\rho_A/a = 5.924$ E-3 and $\rho_B/c = 8.301$ E-3.

Aspect ratio predictions were highly sensitive to the constraint factors chosen. For example, the empirical trend of increasing aspect ratio for initial aspect ratios with $a/c < 1$ observed in Fig. 5 was easily reversed when using the model if inappropriate values of constraint were assumed. This effect is illustrated in Fig. 6, where an aspect ratio evolution simulation generated using the non-uniform constraint $\alpha_A = 3.00$ and $\alpha_B = 2.50$ is compared with that obtained using a uniform average constraint $\alpha_A = \alpha_B = 2.75$ for one of the $R = 0.1$ fatigue tests. Also shown are the corresponding stabilized or steady-state crack opening stress values. A uniform level of crack front constraint resulted in an approximately uniform crack opening stress along the crack front. Under these conditions, the crack was predicted to maintain a constant aspect ratio, in disagreement with the experimental data.

From previous experience with fitting through crack fatigue data, plane stress conditions typically require constraint values $1.00 < \alpha < 1.20$, while plane strain conditions require values $1.80 < \alpha < 2.50$. Consequently, the constraint values required for correlation with the data were larger than expected. This may be a result of the assumed linear constraint variation along the crack front, which over-emphasizes the plane stress contribution, thus reducing the global constraint level. To compensate a reduced global constraint, larger local constraint factors would be needed.

Using $\alpha_A = 3.00$ and $\alpha_B = 2.50$, aspect ratio evolution for loadings with $R = 0.3$ and 0.6 were next predicted and compared with the experimental results from Jolles and Tortoriello. These

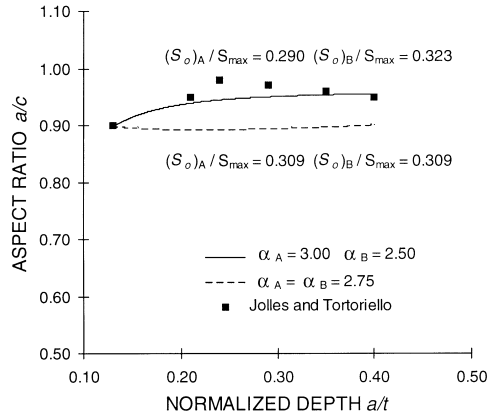

Fig. 6. Effect of constraint definition on aspect ratio evolution, $R = 0.1$.

Table 1. Predicted and measured aspect ratio evolution, $R = 0.3$ and $R = 0.6$

	Initial flaw		Final flaw: Predicted		Final flaw: Measured	
R	a/t	a/c	a/t	a/c	a/t	a/c
0.30	0.16	0.99	0.415	0.933	0.43	0.93
0.30	0.14	0.70	0.439	0.908	0.44	0.92
0.60	0.15	0.99	0.420	0.880	0.42	0.90
0.60	0.15	0.79	0.41	0.864	0.41	0.89

comparisons are given in Table 1. From this table, a good correlation between the predictions and experimental results was obtained.

From Eq. (24), the aspect ratio predictions given are a function of the effective stress intensity factor ranges for points A and B of the surface flaw. These factors are a function of the predicted crack opening stresses S_0 at A and B. With the low applied stress level and high constraint values involved, these crack opening stresses were essentially constant and independent of crack size with, for any one of the four fatigue tests with $R = 0.1$, $(S_0)_A/S_{max} \approx 0.28$ and $(S_0)_B/S_{max} \approx 0.32$.

In terms of flaw shape evolution, earlier studies have shown that crack growth predictions for semielliptical surface flaws cannot be solely predicted by stress intensity factor ranges alone. For example, small initially semicircular flaws have been observed to maintain their semicircular shape under uniform cyclic loading with $R = 0$ despite the fact that the stress intensity factor is $\approx 10\%$ higher at the free surface [4]. Potential reasons for this observation include anisotropic crack growth material behaviour, the lack of a $1/\sqrt{r}$ singularity at the free surface [34] which, from a rigorous viewpoint, invalidates the use of the stress intensity factor at this point, and an increased crack opening value at the free surface as a consequence of the reduced constraint and increased plastic deformation.

Adopting the plasticity-induced closure perspective, differences in the level of crack closure at A and B will alter the shape of a growing crack with the increased level of closure at point B resulting in slower crack growth rates dc/dN relative to da/dN. Conventional crack growth analyses using stress intensity factor ranges may be modified to incorporate the effects of plasticity-induced closure through introduction of a factor β_R, which is related to the crack closure differences at A and B. Using the crack closure parameter U

$$U = \frac{\Delta K_{eff}}{\Delta K} = \frac{1 - (S_0/S_{max})}{1 - R} \tag{25}$$

and assuming $n_A = n_B$ and $C_A = C_B$, Eq. (22) may be written as

$$\frac{da}{dN} = C(U_A \Delta K_A)^n \qquad \frac{dc}{dN} = C(U_B \Delta K_B)^n \tag{26}$$

Defining $\hat{C} = CU_{\mathrm{A}}^{n}$, Eq. (26) may be written

$$\frac{\mathrm{d}a}{\mathrm{d}N} = \hat{C}(\Delta K_{\mathrm{A}})^{n} \qquad \frac{\mathrm{d}c}{\mathrm{d}N} = \hat{C}\left(\frac{U_{\mathrm{B}}}{U_{A}}\Delta K_{\mathrm{B}}\right)^{n} = \hat{C}(\beta_{\mathrm{R}}\Delta K_{\mathrm{B}})^{n} \tag{27}$$

For a small semicircular flaw to remain semicircular during fatigue crack growth, Jolles and Tortoriello [2] estimated $U_{\mathrm{B}}/U_{\mathrm{A}} = 0.911$. In a later effort [3], they measured surface U-values in compact tension specimens with these values used to approximate U_{B}. Their results gave

$$U_{\mathrm{B}} = 0.707 + 0.408R \tag{28}$$

Using this information, Newman and Raju [4] derived the following for semielliptical cracks under uniform constant amplitude loading with $R > 0$

$$\beta_{\mathrm{R}} = \frac{U_{\mathrm{B}}}{U_{\mathrm{A}}} = 0.9 + 0.2R^{2} - 0.1R^{4} \tag{29}$$

For $R < 0$, a value $\beta_{\mathrm{R}} = 0.9$ was suggested. For a small initially semicircular flaw with $a/c = 1.0$, this expression is compared with results from the strip-yield model for both positive and negative R ratios in Fig. 7. From the figure, Eq. (29) is seen to underestimate the level of closure at the deepest point of penetration when compared with the model predictions. The ratio $U_{\mathrm{B}}/U_{\mathrm{A}}$ was also predicted to be a function of applied stress level. The crack opening stresses associated with the β_{R}-values given in Fig. 7 are shown in Fig. 8 for $R = 0.0$. Note that the value $(S_0)_{\mathrm{B}}/S_{\max} = 0.293$ obtained from Eq. (28) compares well with $(S_0)_{\mathrm{B}}/S_{\max} = 0.313$ and 0.296 for stress levels of $S_{\max}/\sigma_0 = 0.25$ and 0.50, respectively, from the strip-yield model. Crack opening stresses are often a function of the type of applied loading as well [23], and thus the β_{R} and opening stresses would possibly change under loadings other than the uniform tension considered. Note also that for the Jolles and Tortoriello data with $R = 0.1$, Eq. (28) gives $(S_0)_{\mathrm{B}}/S_{\max} = 0.327$ and Eq. (29) gives $\beta_{\mathrm{R}} = 0.902$. Use of the strip-yield model for any one of the four fatigue tests with $R = 0.1$ resulted in $(S_0)_{\mathrm{A}}/S_{\max} \approx 0.28$, $(S_0)_{\mathrm{B}}/S_{\max} \approx 0.32$, and $\beta_{\mathrm{R}} = 0.944$. Thus, opening stress predictions at the free surface compared well with the experimental data, while the predicted opening stress at the deepest point of penetration was larger than that estimated by Jolles and Tortoriello.

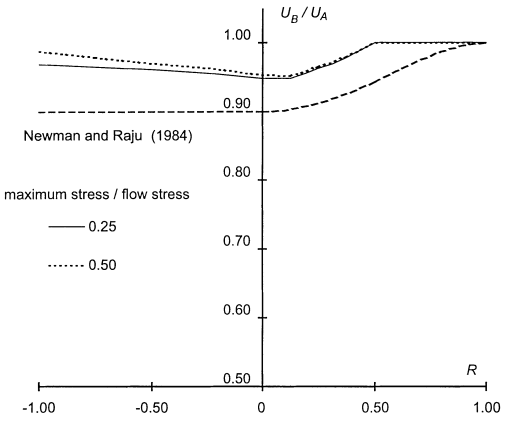

Fig. 7. Predicted closure behaviour for a small semicircular flaw under uniform tension.

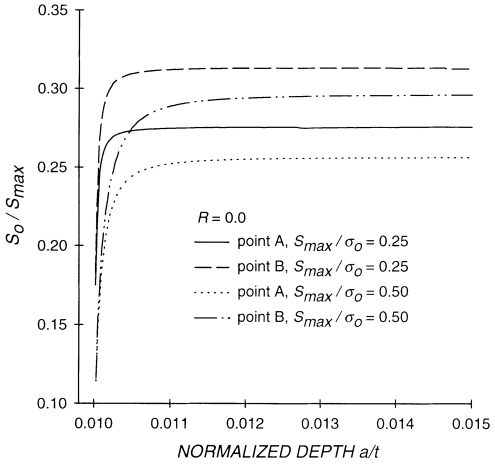

Fig. 8. Predicted opening stresses for a small semicircular flaw under uniform tension.

Equation (29) was derived using estimates and measurements of surface flaw crack closure presented by Jolles and Tortoriello [2,3]. Flaw shape evolution data also presented by these same researchers [3] were used to calibrate/validate the strip-yield model. Given that Eq. (29) and the model predicted different relative closure behaviour, as observed in Fig. 7, it is apparent that the validation of closure-based models using flaw shape evolution data does not infer a crack opening stress validation. Similarly, validation using crack opening measurements may not ensure accurate flaw shape evolution prediction as a consequence of potential anisotropic crack growth material behaviour and the uncertain nature of the free surface singularity.

CONCLUDING REMARKS

A slice synthesis methodology has been employed to construct a modified strip-yield model for the semielliptical surface flaw, enabling a prediction of plasticity-induced closure along the crack front and subsequent fatigue crack growth. Using coupled strip-yield model analyses, concurrent crack closure assessments were performed for the surface flaw at both the deepest point of penetration and the surface point. Slice synthesis methodologies have previously been limited to the computation of stress intensity factor and elastic crack surface displacement values.

Crack opening stress predictions for a semicircular flaw under uniform cyclic tension were compared with results from a finite element study [10], in which the flaw was assumed to grow with a fixed aspect ratio. Opening stresses from the finite element model were significantly lower than those computed using the strip-yield model. The finite element mesh was relatively course in the crack front region, and analyses incorporating more refined meshes are needed to make valid comparisons with the strip-yield model. Finite element meshes must be sufficiently refined such that crack growth increments comprise a small portion of the plastic zone along the crack front. Finite element models must also consider the evolution of the flaw shape and not be restricted to fixed aspect ratios.

Predictions of crack shape development under cyclic loading were compared with experimental data for 2024-T351 aluminium alloy specimens under uniform constant amplitude cyclic loading at stress ratio values R of 0.1, 0.3 and 0.6. The model was developed assuming the surface flaw was small. However, predictions were shown to correlate well with experimental data, with this data considering flaws as deep as $a = 0.45t$, where t is the specimen thickness. Opening stress predictions at the free surface compared well with the experimental data, while the predicted opening stress at the deepest point of penetration was larger than that estimated by Jolles and Tortoriello [2,3]. This may be a result of the approximate nature of the assumed crack front constraint distribution, as given in this paper.

Plastic zone crack front constraint factors have been treated as fitting parameters using experimental crack shape development data for $R = 0.1$. The resulting values of 3.00 and 2.50, for the deepest point of penetration and the surface point, respectively, were larger than expected. This may also be a result of the assumed linear constraint variation along the crack front, which overemphasizes the plane stress contribution, thus reducing the global constraint level.

To rigorously characterize the distribution of constraint along the crack front, elastic–plastic finite element analyses are needed. Constraint factors represent the effects of localized plastic deformation, and the distribution of constraint will also be a function of applied load. However, modified strip-yield model constraint factors also indirectly consider other closure mechanisms, e.g. roughness-induced closure and closure from corrosion products or fretting debris, and are thus best treated as fitting parameters. Consequently, while finite element analyses will enable the

distribution of constraint to be determined, the actual magnitudes must continue to be found using fatigue crack growth data, as performed in this study.

Acknowledgement—The author wishes to thank Dr J. C. Newman of the NASA Langley Research Center for the guidance and encouragement received from many helpful discussions.

REFERENCES

1. N. A. Fleck, I. F. C. Smith and R. A. Smith (1983) Closure behavior of surface cracks. *Fatigue Engng Mater. Struct.* **6,** 225–239.
2. M. Jolles and V. Tortoriello (1983) Geometry variations during fatigue growth of surface flaws. In: *Fracture Mechanics: 14th Symposium—Vol. I: Theory and Analysis*, *ASTM STP 791*, pp. I297–I307.
3. M. Jolles and V. Tortoriello (1984) Effects of constraint variation on the fatigue growth of surface flaws. In: *Fracture Mechanics: 15th Symposium*, *ASTM STP 833*, pp. 300–311.
4. J. C. Newman and I. S. Raju (1984) Prediction of fatigue crack-growth patterns and lives in three-dimensional cracked bodies. In: *Advances in Fracture Research, Proceedings of the 6th Int. Conf. of Fracture* (*ICF6*), Pergamon Press, pp. 1597–1608.
5. R. Foroughi and J. C. Radon (1988) Crack closure Behavior of surface cracks under bending loading. In: *Mechanics of Fatigue Crack Closure*, *ASTM STP 982*, pp. 260–269.
6. J. H. Kim and J. H. Song (1992) Crack growth and closure behavior of surface cracks under axial loading. *Fatigue Fract. Engng Mater. Struct.* **15,** 477–489.
7. A. Carpinteri (1994) Propagation of surface cracks under cyclic loading. In: *Handbook of Fatigue Crack Propagation in Metallic Structures*, Elsevier Science, pp. 653–705.
8. W. Elber (1970) Fatigue crack closure under cyclic tension. *Engng Fracture Mech.* **2,** 37–45.
9. W. Elber (1971) The significance of fatigue crack closure. In: *Damage Tolerance in Aircraft Structures*, *ASTM STP 486*, pp. 230–242.
10. R. G. Chermahini, B. Palmberg and A. F. Blom (1993) Fatigue crack growth and closure behavior of semicircular and semi-elliptical surface flaws. *Int. J. Fatigue* **15,** 259–263.
11. J. C. Newman (1981) A crack-closure model for predicting fatigue crack growth under aircraft spectrum loading. In: *Methods and Models for Predicting Fatigue Crack Growth Under Random Loading*, *ASTM STP 748*, pp. 53–84.
12. H. D. Dill and C. R. Saff (1977) Analysis of crack growth following compressive high loads based on crack surface displacements and contact analysis. In: *Cyclic Stress–Strain and Plastic Deformation Aspects of Fatigue Crack Growth*, *ASTM STP 637*, pp. 141–152.
13. B. Budiansky and J. W. Hutchinson (1978) Analysis of closure in fatigue crack growth. *J. Appl. Mech.* **45,** 267–276.
14. J. C. Newman (1984) A crack opening stress equation for fatigue crack growth. *Int. J. Fracture* **24,** R131–R135.
15. F. K. Ibrahim (1986) A study of the effect of mechanical variables on fatigue crack closure and propagation. Ph.D. Dissertation, University of Waterloo.
16. A. U. de Koning and G. Liefting (1988) Analysis of crack opening behavior by application of a discretized strip yield model. In: *Mechanics of Fatigue Crack Closure*, *ASTM STP 982*, pp. 437–458.
17. H. Nakamura and H. Kobayashi (1988) Analysis of fatigue crack closure caused by asperities using the modified Dugdale model. In: *Mechanics of Fatigue Crack Closure*, *ASTM STP 982*, pp. 459–474.
18. D. Chen and H. Nisitani (1988) Analytical and experimental study of crack closure behavior based on an S-shaped unloading curve. In: *Mechanics of Fatigue Crack Closure*, *ASTM STP 982*, pp. 475–488.
19. S. R. Daniewicz (1991) Conception and development of improved analytical prediction models for fatigue induced tooth breakage due to cyclic bending in spur gear teeth. Ph.D. Dissertation, Ohio State University.
20. G. S. Wang and A. F. Blom (1991) A strip model for fatigue crack growth predictions under general load conditions. *Engng Fracture Mech.* **40,** 507–533.
21. S. R. Daniewicz, J. A. Collins and D. R. Houser (1994) An elastic–plastic analytical model for predicting fatigue crack growth in arbitrary edge-cracked two-dimensional geometries with residual stress. *Int. J. Fatigue* **16,** 123–133.
22. J. C. Newman (1995) Fatigue-life prediction using a crack-closure model. *J. Engng Mater. Tech.* **117,** 433–439.

23. S. R. Daniewicz and J. M. Bloom (1996) An assessment of geometry effects on plane stress fatigue crack closure using a modified strip-yield model. *Int. J. Fatigue* **18,** 483–490.
24. W. Zhao, X. R. Wu and M. G. Yan (1989) Weight function method for three dimensional crack problems—I. Basic formulation and application to an embedded elliptical crack in finite plates. *Engng Fracture Mech.* **34,** 593–607.
25. C. Mattheck and F. Görner (1984) Leak prediction by use of a generalized Dugdale model for semi-elliptical surface flaws in plates under tension loading. *Proc. 5th European Conf. on Fracture*, Portugal.
26. S. R. Daniewicz (1994) Accurate and efficient numerical integration of weight functions using Gauss–Chebyshev quadrature. *Engng Fracture Mech.* **48,** 541–544.
27. W. T. Fujimoto (1976) Determination of crack growth and fracture toughness parameters for surface flaws emanating from fastener holes. In: *Proc. AIAA/ASME/SAE 17th Structures, Structural Dynamics, and Material Conf.*, King of Prussia, PA, pp. 522–531.
28. C. R. Saff and K. B. Sanger (1984) Part-through flaw stress intensity factors developed by a slice synthesis technique. In: *Fracture Mechanics: 15th Symposium*, *ASTM STP 833*, pp. 24–43.
29. W. Zhao, X. R. Wu and M. G. Yan (1989) Weight function method for three dimensional crack problems—II. Application to surface cracks at a hole in finite thickness plates under stress gradients. *Engng Fracture Mech.* **34,** 609–624.
30. W. Zhao and M. A. Sutton (1995) Elastic solutions for corner cracks undergoing uniform displacement-controlled loading. *Int. J. Fracture* **70,** 335–346.
31. D. S. Dugdale (1960) Yielding of steel sheets containing slits. *J. Mech. Physics Solids* **8,** 100–104.
32. D. J. Ayres (1970) A numerical procedure for calculating stress and deformation near a slit in a three-dimensional elastic–plastic solid. *Engng Fracture Mech.* **2,** 87–106.
33. J. C. Newman and I. S. Raju (1986) Stress intensity factor equations for cracks in three-dimensional finite bodies subjected to tension and bending loads. In: *Computational Methods in the Mechanics of Fracture* (Edited by S. N. Atluri), Vol. 2, Elsevier Science, Amsterdam.
34. D. M. Parks (1990) A surface crack review: elastic and elastic–plastic behavior. In: *Surface Crack Growth: Models, Experiments and Structures*, *ASTM STP 1060*, pp. 9–33.
35. X. R. Wu and A. J. Carlsson (1991) *Weight Functions and Stress Intensity Factor Solutions*, Pergamon Press, Oxford.
36. A. P. Parker (1981) *The Mechanics of Fracture and Fatigue*, E. & F. N. Spon, London.
37. H. Tada, P. C. Paris and G. R. Irwin (1985) *The Stress Analysis of Cracks Handbook*, Paris Production & Del Research, St. Louis, Missouri.

APPENDIX

Weight functions

For the edge-crack in a half plane, the following weight function was used [35]

$$m(x,a) \cong \frac{1}{\sqrt{2\pi(a-x)}}\left[2.00 + 0.9788(1-x/a) + 1.1101(1-x/a)^2 - 0.3194(1-x/a)^3 - 0.1017(1-x/a)^4\right] \tag{A1}$$

For the centre through crack in an infinite body under symmetrical loading, an exact weight function is available [36]

$$m(y,c) = \frac{1}{\sqrt{2\pi(c-y)}}\,\frac{2\sqrt{2}}{\sqrt{1+y/c}} \tag{A2}$$

Calibration process for surface flaw strip-yield model

Consider an embedded circular crack with radius b in an infinite body under a uniform tension σ, as shown in Fig. A1. An elastic–perfectly plastic material is assumed with modulus E and flow stress σ_0. The plastic zone size ρ and crack tip opening displacement δ_t may be written as [37]

$$\frac{b}{\rho+b} = \sqrt{1-\left(\frac{\sigma}{\sigma_0}\right)^2} \tag{A3}$$

$$\delta_t = \frac{8(1-\nu^2)}{\pi E}\,\sigma_0 b\left(1-\frac{b}{\rho+b}\right) \tag{A4}$$

Consider modelling this crack using a slice synthesis methodology. Both the primary and spring slices (a and c slices)

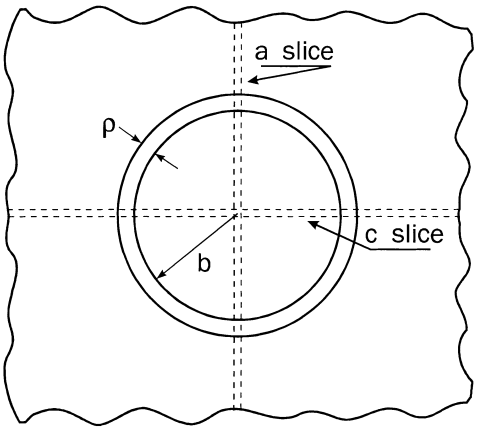

Fig. A1. Embedded circular crack.

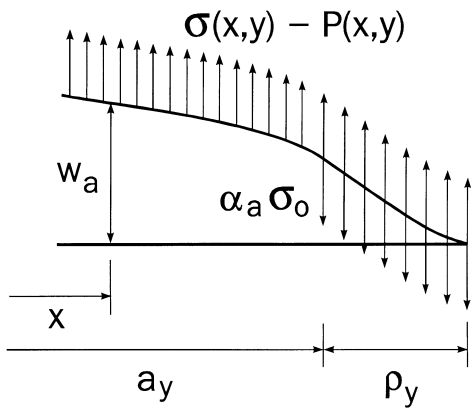

Fig. A2. Primary slice crack surface displacement.

constitute centre-cracked panels with a crack length of $2b$. The primary slice exhibits a modulus E and flow stress σ_0, while the spring slice has a modulus E_S and flow stress σ_{0S}. The primary slice is assumed to be under a uniform stress $\sigma - P$, while the spring slice is assumed to be under a uniform stress P. The uniform stress P is a consequence of the uniform applied stress σ [24,27]. The plastic zone sizes for the primary and spring slices may be written as follows

$$\frac{b}{b+\rho_a} = \cos\left(\frac{\pi}{2}\frac{\sigma - P}{\sigma_0}\right) \qquad \frac{b}{b+\rho_c} = \cos\left(\frac{\pi}{2}\frac{P}{\sigma_{0S}}\right) \tag{A5}$$

The crack tip opening displacements may be written as

$$\delta_{ta} = \frac{8(1-\nu^2)}{\pi E}\sigma_0 b \ln\left(\frac{b+\rho_a}{b}\right) \qquad \delta_{tc} = \frac{8(1-\nu^2)}{\pi E_S}\sigma_{0S} b \ln\left(\frac{b+\rho_c}{b}\right) \tag{A6}$$

The primary and spring slices must exhibit equal plastic zone sizes. From Eq. (A5)

$$\frac{\sigma - P}{\sigma_0} = \frac{P}{\sigma_{0S}} \tag{A7}$$

The primary and spring slices must also have equal crack tip opening displacements. Using Eq. (A6) this yields

$$\frac{\sigma_{0S}}{\sigma_0} = \frac{E_S}{E} \tag{A8}$$

From Eqs (A7) and (A8)

$$P = \frac{\sigma}{1 + E/E_S} \tag{A9}$$

To calibrate the model, the actual crack tip opening displacement must equal that given by the primary (or spring) slice with $\delta_t = \delta_{ta}$. This requirement gives

$$\frac{\rho}{b} = \frac{1}{\dfrac{1}{\ln(1+\rho_a/b)} - 1} \tag{A10}$$

Equation (A10) establishes a correlation between slice plastic zone sizes and actual plastic zones sizes for a circular flaw. Following this general form, for a semielliptical flaw, the correlations given as Eqs (14) and (15) were assumed.

Surface flaw displacements

Figure A2 illustrates the crack surface displacement for a primary slice passing through a semielliptical surface flaw. This slice exhibits a plastic zone size ρ_y and a constraint factor α_a. For a dummy crack length α with $\alpha < a_y$, the stress intensity factor may be written as

$$K(\alpha) = \int_0^\alpha [\sigma(\xi, y) - P(\xi, y)] m_a(\xi, \alpha)\, d\xi \tag{A11}$$

For $\alpha \geqslant a_y$, the slice stress intensity factor is given by

$$K(\alpha) = \int_0^{\alpha} [\sigma(\xi, y) - P(\xi, y)] m_a(\xi, \alpha)\, d\xi - \int_{a_y}^{\alpha} \alpha_a \sigma_0 m_a(\xi, \alpha)\, d\xi \tag{A12}$$

Using Eqs (A11) and (A12), the crack surface displacement for a given x may be written as

$$w_a = \frac{1}{E} \int_x^{a_y + \rho_y} K(\alpha) m_a(x, \alpha)\, d\alpha \tag{A13}$$

$$w_a = \frac{1}{E} \int_x^{a_y} \left\{ \int_0^{\alpha} [\sigma(\xi, y) - P(\xi, y)] m_a(\xi, \alpha)\, d\xi \right\} m_a(x, \alpha)\, d\alpha + \frac{1}{E} \int_{a_y}^{a_y + \rho_y} \left\{ \int_0^{\alpha} [\sigma(\xi, y) - P(\xi, y)] m_a(\xi, \alpha)\, d\xi - \int_{a_y}^{\alpha} \alpha_a (\sigma_0 m_a(\xi, \alpha)\, d\xi \right\} m_a(x, \alpha)\, d\alpha \tag{A14}$$

which was given as Eq. (16). In a similar fashion, an equation for the spring slice crack surface displacement may be written. This result was given as Eq. (17).

Determination of shear traction

The slice crack surface displacements w_a and w_c were given as Eqs (16) and (17). For compatibility, $w_a = w_c$. Using the compatibility requirement in conjunction with Eq. (20)

$$Y(x, y) = \sum_{i=1}^{14} \lambda_i X_i(x, y) \tag{A15}$$

$$Y(x, y) = \int_x^{a_y} \int_0^{\alpha} \sigma(\xi, y) m_a(\xi, \alpha) m_a(x, \alpha)\, d\xi\, d\alpha + \int_{a_y}^{a_y + \rho_y} \int_0^{\alpha} \sigma(\xi, y) m_a(\xi, \alpha) m_a(x, \alpha)\, d\xi\, d\alpha - \int_{a_y}^{a_y + \rho_y} \int_{a_y}^{\alpha} \alpha_a \sigma_0 m_a(\xi, \alpha) m_a(x, \alpha)\, d\xi\, d\alpha + \frac{E}{E_s} \int_{c_x}^{c_x + \rho_x} \int_{c_x}^{\gamma} \alpha_c \sigma_{0S} m_c(\psi, \gamma) m_c(y, \gamma)\, d\psi\, d\gamma \tag{A16}$$

$$X_i(x, y) = \int_x^{a_y} \int_0^{\alpha} p_i(\xi, y) m_a(\xi, \alpha) m_a(x, \alpha)\, d\xi\, d\alpha + \frac{E}{E_s} \int_y^{c_x} \int_0^{\gamma} p_i(x, \psi) m_c(\psi, \gamma) m_c(y, \gamma)\, d\psi\, d\gamma + \int_{a_y}^{a_y + \rho_y} \int_0^{\alpha} p_i(\xi, y) m_a(\xi, \alpha) m_a(x, \alpha)\, d\xi\, d\alpha + \frac{E}{E_s} \int_{c_x}^{c_x + \rho_x} \int_0^{\gamma} p_i(x, \psi) m_c(\psi, \gamma) m_c(y, \gamma)\, d\psi\, d\gamma \tag{A17}$$

Consider m arbitrary but evenly distributed points within the semielliptical flaw boundary. If Eq. (A15) is written for each of these points, then a system of m equations for the 14 unknown λ_i results. This system may be written as

$$\{Y\} = [X]\{\lambda\} \tag{A18}$$

where $\{Y\}$ is a $m \times 1$ vector, $\{\lambda\}$ is a 14×1 vector, and $[X]$ is a $m \times 14$ matrix. As discussed by Zhao *et al.* [24], for a prescribed m with $m > 14$, Eq. (A18) represents an over-determined system of equations. This system was solved for the unknown vector $\{\lambda\}$ using singular value decomposition. A value of $m = 35$ was used. A value of 34 was used by Zhao *et al.* [24].